Population Balance Modeling of Antibodies Aggregation Kinetics

Paolo Arosio, Simonetta Rima, Marco Lattuada,[||] and Massimo Morbidelli*

Institute for Chemical and Bioengineering, Department of Chemistry and Applied Biosciences, ETH Zurich, 8093 Zurich, Switzerland

[||]Adolphe Merkle Institute, University of Fribourg, CH-1723 Marly 1, Switzerland

S *Supporting Information*

ABSTRACT: The aggregates morphology and the aggregation kinetics of a model monoclonal antibody under acidic conditions have been investigated. Growth occurs via irreversible cluster—cluster coagulation forming compact, fractal aggregates with fractal dimension of 2.6. We measured the time evolution of the average radius of gyration, $\langle R_g \rangle$, and the average hydrodynamic radius, $\langle R_h \rangle$, by in situ light scattering, and simulated the aggregation kinetics by a modified Smoluchowski's population balance equations. The analysis indicates that aggregation does not occur under diffusive control, and allows quantification of effective intermolecular interactions, expressed in terms of the Fuchs stability ratio (W). In particular, by introducing a dimensionless time weighed on W, the time evolutions of $\langle R_h \rangle$ measured under various operating conditions (temperature, pH, type and concentration of salt) collapse on a single master curve. The analysis applies also to data reported in the literature when growth by cluster—cluster coagulation dominates, showing a certain level of generality in the antibodies aggregation behavior. The quantification of the stability ratio gives important physical insights into the process, including the Arrhenius dependence of the aggregation rate constant and the relationship between monomer—monomer and cluster—cluster interactions. Particularly, it is found that the reactivity of non-native monomers is larger than that of non-native aggregates, likely due to the reduction of the number of available hydrophobic patches during aggregation.
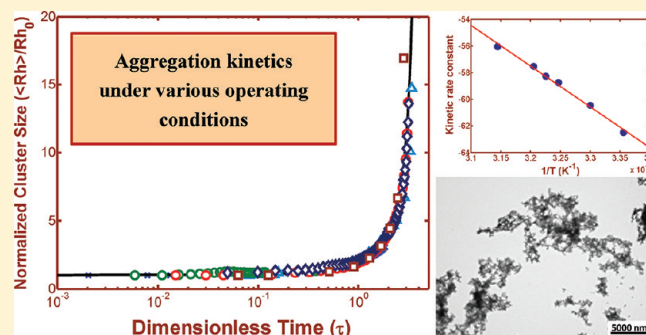
INTRODUCTION

Protein self-assembling is widely investigated for its implications in several human diseases[1] as well as in the industrial processes for the production of therapeutic proteins.[2,3] During the manufacturing process the proteins are in fact exposed to several types of stresses, which often induce aggregation and loss of valuable product.[4]

A large number of experimental investigations have been reported aimed at the fundamental description of the aggregation process and the individuation of the key factors responsible for protein stability.[5−9] Many different types of aggregates have been observed, ranging from oligomers to large precipitates.[10−13] Such aggregates are the final or intermediate products of several possible aggregation mechanisms and pathways.[14] Despite their large heterogeneity most aggregation behaviors can be included in an universal multistep Lumry—Eyring modified model.[15] The aggregation scheme involves the formation of an aggregating-prone intermediate in a non-native state, reversible oligomer formation, nucleation of reversible or irreversible aggregates, and growth to larger aggregates. The latter step can occur either by cluster—cluster coagulation or by monomer addition to preformed nuclei. The specific protein and the operating conditions under consideration determine the features of the individual steps and, consequently, the overall mechanism. Moreover, different path-ways are not mutually exclusive and could also occur simultaneously.[16]

Mathematical models of aggregation kinetics represent a useful tool for the mechanistic description of the process,[17−19] as well as for product shell-life prediction,[20] which represents a great challenge in pharmaceutical industry. Roberts and co-workers identified the most common mechanisms observed in protein aggregation[21,22] and developed a comprehensive kinetic model based on mass action law.[15,23,24] The developed models were applied to describe the aggregation behavior of several model therapeutic proteins, including α-chymotrypsinogen A,[25,26] stimulating factors,[27] and monoclonal antibodies.[28−30]

Many protein solutions share features of sol colloidal dispersions,[31] whose aggregation kinetics is commonly described by models based on population balance equations (PBEs). Recently, PBEs have been applied to the kinetics of formation of amyloid fibrils.[32−34] The application of PBEs to protein aggregation kinetics has several motivations: (1) it provides quantitative mechanistic insights into the single steps constituting the overall process; (2) from the evaluated aggregation rate coefficients (kernels), quantitative information on average protein—protein interactions can be obtained.

Ideally, the time evolution of the aggregate size distribution can be described a priori by means of PBE simulations provided that protein—protein interaction potential is properly charac-

terized. For lyophobic colloids, quantification of potential interactions is successfully achieved by mean filed approaches such as the DLVO theory and its modifications.[31] For complex, lyophilic macromolecules, such as proteins, the situation is more challenging.[35] Protein surfaces exhibit anisotropic distribution of charges and simultaneous presence of hydrophobic and hydrophilic patches. Donnan effects and additional interactions, including depletion, hydrophobic and solvation forces, must be accounted for in protein interaction potential.[36] Moreover, strong intermolecular forces are often confined to specific patches of the protein surface.[37] As a consequence, structure stability is strongly interconnected to colloidal stability, and the two contributions superimpose in determining aggregation propensity.[38] Given such considerations, the detailed description of the protein structure appears fundamental to properly catch protein−protein interactions. However, despite the mentioned limitations, mean field models are often used to describe average protein−protein interactions responsible for aggregation, particularly when electrostatic interactions dominate.[39] Globular proteins are particularly suitable for this approach: Randolph, Carpenter and coauthors applied the colloidal formalism to describe several model proteins including Fc fusion protein,[40] human stimulating factor,[41] human interleukin-1 receptor antagonist[42] and *Bacillus halmapalus* α-amylase.[43] Additionally, also short peptides and amyloidogenic proteins have been modeled along these lines.[44,45]

In this work, we investigated the aggregates morphology and the aggregation kinetics of a model monoclonal antibody. Under the considered conditions, the IgG aggregates via a two-step process: reversible nucleation of oligomers followed by irreversible cluster−cluster coagulation. We developed a comprehensive population balance model including both steps of aggregation. By fitting the model simulations to experimental data, we quantified the effective monomer−monomer and aggregate-aggregate interaction potentials as a function of several operating conditions. Moreover, the analysis has been extended to data reported in the literature for other systems where however growth by cluster−cluster coagulation dominates over chain polymerization, similarly to the one considered in this work.

MATERIAL AND METHODS

Materials. The monoclonal antibody considered in this work is an IgG2 with molecular weight ∼150 kDa and with isoelectric point (pI) between 7.35 and 8.15. A mother antibody solution at 45 g/L in 10 mM sodium citrate, 50 mM NaCl, 150 mM sucrose at pH 6.0 was stored at 4 °C.

The solutions for aggregation studies were prepared by manually diluting the mother solution to 1 g/L by selected buffer solutions. This represents the typical concentration value of the protein in purification downstream processes. For each condition three repetitions were performed and average values are reported. All buffers for aggregation studies were filtered using 0.25 μm cutoff sterile syringe filters Pall Acrodisc 32 mm (PALL Life Sciences, NY). 0.5 g/L of sodium azide was added to all solutions to prevent formation and proliferation of bacterial growth. All chemicals were supplied by Sigma-Aldrich (Buchs, Switzerland).

Light Scattering. Dynamic light scattering (DLS) was measured at a fixed angle of $\theta = 173°$ using a Zetasizer Nano (Malvern, U.K.) with laser beam of wavelength $\lambda_0 = 633$ nm.

Static light scattering (SLS) measurements were performed using a goniometer, BI-200SM (Brookhaven Instruments, Holtsville, NY) covering angles from $\theta = 16$ to 150°. A solid-state laser, Ventus LP532 (Laser Quantum, Manchester, U.K.), with a wavelength $\lambda_0 = 532$ nm was used as the light source. With the same instrument, DLS was measured at a fixed angle of $\theta = 145°$.

Dynamic and static light scattering were also measured with a Dawn Heleos II detector (Wyatt, Dernbach, Germany) with laser beam of wavelength $\lambda_0 = 658$ nm covering angles from $\theta = 14$ to 163°. Dynamic light scattering (DLS) was measured at a fixed angle of $\theta = 90°$.

Small angle light scattering (SALS) was performed on a Mastersizer 2000 (Malvern, U.K.) covering angles from $\theta = 0.02$ to 40° and with a light source with wavelength $\lambda_0 = 633$ nm.

Atomic Force Microscopy. Here, 10 μL each of 150-fold diluted samples were spotted on a freshly cleaved mica surface for 30 s before washing with Milli-Q (Milli-pore) deionized water to remove unattached material and gently drying under nitrogen flux. Samples were imaged at room temperature by a Nanoscope IIIa (Digital Instrument, USA) operating in tapping mode. Scan rate of 0.8 Hz and antimony doped silicon cantilevers with resonance frequency in the range 325−382 kHz and tip radius of 8 nm (Veeco, Plainview, NY) were used.

Transmission Electron Microscopy. Samples for transmission electron microscopy (TEM) were loaded on a carbon grid (Quantifoil, Germany) and negative stained with a 2% uranyl acetate aqueous solution. Pictures were recorded on a FEI Morgagni 268.

RESULTS AND DISCUSSION

Aggregation Kinetics and Structure Morphology. The aggregation kinetics of the model IgG2 at various operating conditions has been measured by in situ dynamic light scattering (DLS). DLS measures the hydrodynamic radius of particles diffusing in solution, and aggregation can be observed by the increase of the average size of the aggregates distribution. Given the small size of the antibody molecule, the intensity has been recorded in the backscattering model at fixed angle, 173°, to avoid interference of large impurities. The pH effect was investigated selecting as reference system 1 g/L protein solution in 25 mM citric acid buffer with 0.15 M Na₂SO₄ at 37 °C. The time evolution of the average hydrodynamic radius, $\langle R_h \rangle$, for various pH values is shown in Figure 1a. It is seen that by decreasing the pH from 4.5 to 3.25 the oligomers become progressively more unstable, but in all cases limited aggregation is observed. At the critical pH value of 3.0, the aggregation kinetics increases dramatically: aggregates increase their size until they become insoluble and, eventually, precipitate. Because of aggregate sedimentation, the light scattering signal decreases when the average $\langle R_h \rangle$ reaches a value of about 200 nm. Therefore, we only considered smaller sizes, corresponding to non sedimentating conditions. It is found that the aggregation kinetics at pH 3.0 is very sensitive to temperature (Figure 1b) and type of salt (Figure 1c). The anion effect on the coagulation rate at 37 °C follows the order: $NO_3 > SO_4 > Cl > H_2PO_4$. Notably, the same ranking was previously observed for the coagulation of a IgE light chain fragment at low pH.[46]

The morphology of the formed aggregates during incubation at several temperatures and with different salts has been investigated by transmission electron microscopy (TEM) and
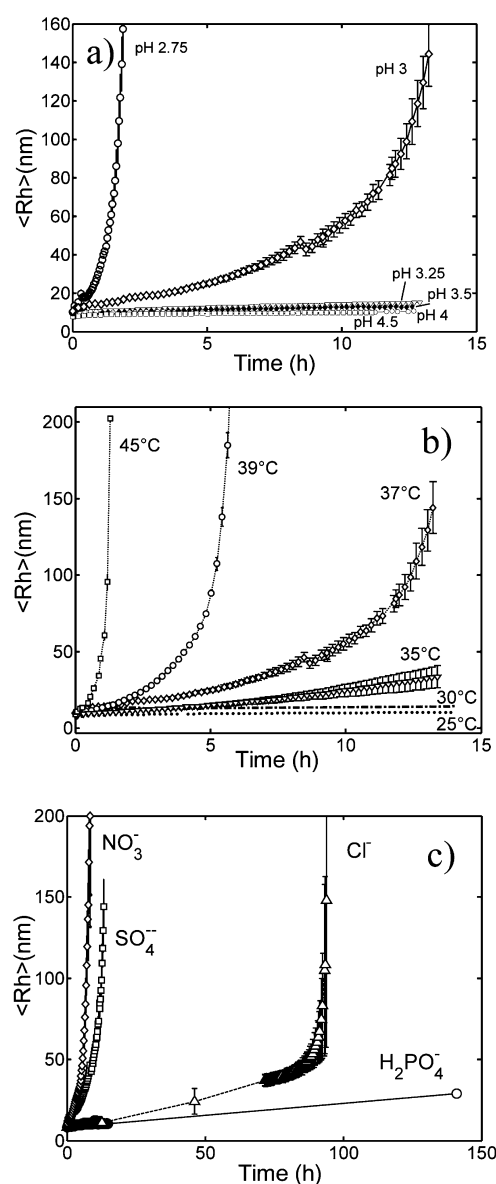
Figure 1. (a) Time evolution of the average hydrodynamic radius, $\langle R_h \rangle$, measured by dynamic light scattering for a 1 g/L mAb solution in 25 mM citric acid buffer with 0.15 M Na_2SO_4 at various pH values and 37 °C; (b) same as part a but at pH 3.0 and different various temperatures; (c) same as a) but at pH 3.0 and 37 °C with 0.15 M of various different counterions.

Figure 2. (a) AFM picture of 1 g/L mAb solution in 25 mM citric acid buffer with 0.15 M Na_2SO_4 at 37 °C and pH 3.0 after 6 h; (b) TEM picture of 1 g/L mAb solution in 25 mM citric acid buffer with 0.5 M NaCl at 25 °C and pH 3.0 after 1 month.

by atomic force microscopy (AFM), which offered a better resolution for small species (few tens of nm) with respect to TEM. 1 g/L protein solution in 25 mM citric acid buffer at pH 3.0 was selected as reference condition. With illustrative purposes, in Figure 2a the AFM picture of a sample taken after 6 h incubation at 37 °C with 0.15 M Na_2SO_4 is shown, indicating the presence of globular aggregates with radius of about 25 nm, consistent with DLS measurements (Figure 1a), and similar in shape to intermediate aggregates reported in the literature.[47] When aggregation proceeds further, irregular, amorphous aggregates are formed, as seen in the TEM picture in Figure 2b, which corresponds to a sample after 1 month incubation at 25 °C with 0.5 M NaCl. Also in this case, the sizes shown by TEM are consistent with the hydrodynamic radius of about 60 nm given by DLS, although the irregular shape and the heterogeneity of the aggregates complicate the comparison.
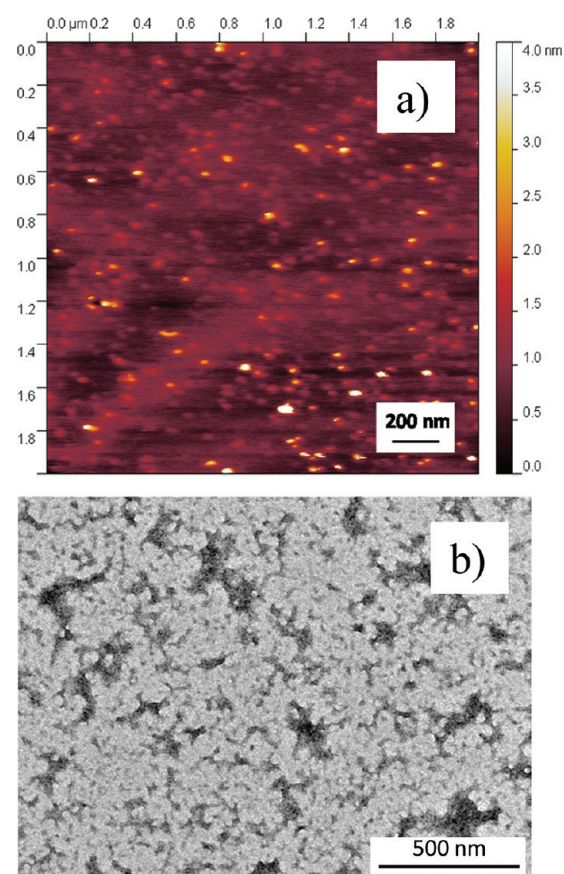
Moreover, the drying procedure required by the microscopy technique could affect the aggregate size, and therefore the comparison between the sizes obtained by microscopy and DLS must be taken only as indicative. Finally, TEM pictures of samples after 24 h incubation at 37 °C with 0.15 M of different salts are reported in Figure 3, where fractal like clusters appear with relatively large compactness.

The fractal behavior of the clusters was proved by small angle light scattering (SALS), which gives information about the structure factor, $S(q)$, of the clusters:

$$S(q) = \frac{I(q)}{I(0)P(q)} \qquad (1)$$

Here $I(q)$ is the angle-dependent scattered intensity, $I(0)$ is the intensity at zero angle, $P(q)$ is the form factor of the primary particles and q is the scattering vector defined as:

$$q = \frac{4\pi n}{\lambda_0}\sin\left(\frac{\theta}{2}\right) \qquad (2)$$

where θ is the scattering angle, n is the refractive index of the solvent and λ_0 is the wavelength of the laser beam. The light scattering has been measured in the small angle region since this angle interval is suitable for the analysis of aggregates with size in the range of several micrometers, which is the characteristic size of the IgG aggregates obtained at the end of the process. For such large clusters, the power-law regime of
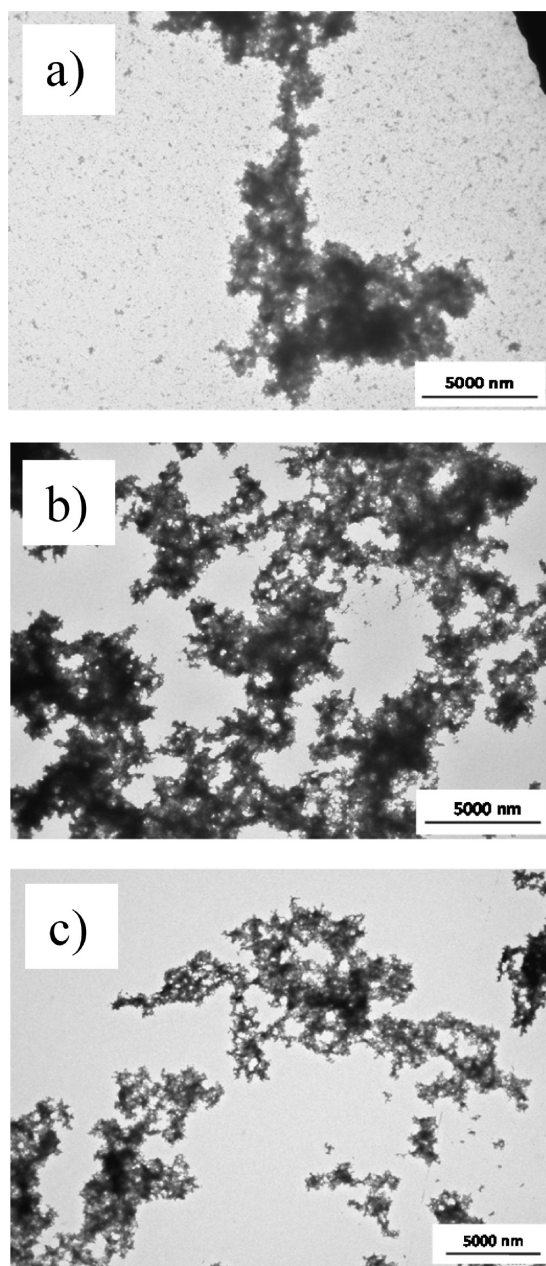
Figure 3. TEM pictures of 1 g/L mAb solution after 24 h incubation in 25 mM citric acid buffer at 37 °C and pH 3.0, with 0.15 M solution of NaCl (a), Na_2SO_4 (b), and $NaNO_3$ (c).

the average structure factor leads to an estimate of the fractal dimension, D_f:

$$S(q) \sim q^{-D_f}, \quad \text{for } 1/\langle R_g \rangle \ll q \ll 1/R_P \quad (3)$$

Here R_P is the radius of the primary particle inside the cluster and $\langle R_g \rangle$ is the average radius of gyration of the cluster distribution. In Figure 4 the structure factor of a sample after 12 h of incubation at 37 °C with 0.15 M Na_2SO_4 is shown. From the fitting in the power-law regime a fractal dimension equal to 2.6 can be evaluated. Such value is in good agreement with the value of D_f = 2.56 reported in the literature for antibody aggregates.[48] Moreover, D_f = 2.6 corresponds to quite compact structures, which is consistent with the TEM pictures shown in Figure 3.
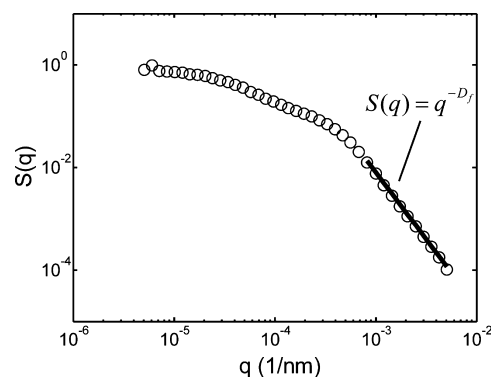

Figure 4. Structure factor of a 1 g/L protein sample after 24 h incubation in 25 mM citric acid buffer at 37 °C and pH 3.0, with 0.15 M Na_2SO_4. From the fitting in the power-law regime a fractal dimension D_f = 2.6 can be evaluated.

From the fractal dimension and $\langle R_h \rangle$ measured by DLS, the aggregate average molecular weight can be evaluated according to the following scaling:

$$\langle MW \rangle \simeq MW_0 \left(\frac{\langle R_h \rangle}{R_0} \right)^{D_f} \quad (4)$$

Considering D_f = 2.6, we compare the values evaluated with eq 4 to the molecular weights directly measured by static light scattering. In Figure 5, the comparison is reported for a 1 g/L mAb solution in 25 mM citric acid buffer with 0.15 M Na_2SO_4 at 25 °C (Figure 5a), and with 0.15 M NaCl at 37 °C (Figure 5b): the values measured by SLS are reasonably in agreement with the ones estimated from eq 4.
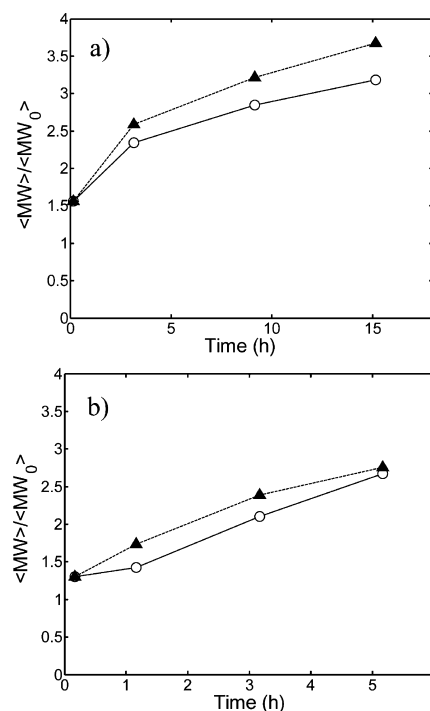

Figure 5. Comparison between normalized average number molecular weight as a function of time measured directly by static light scattering (▲) and estimated from DLS data using eq 4 (○) for a 1 g/L mAb solution in 25 citric acid buffer at pH 3.0 with (a) 0.15 M Na_2SO_4 at 25 °C and (b) with 0.15 M NaCl at 37 °C.

The time evolution of the structure factor during aggregation has been analyzed by static light scattering, as reported in Figure 6. The signal has been recorded in the wide-angle
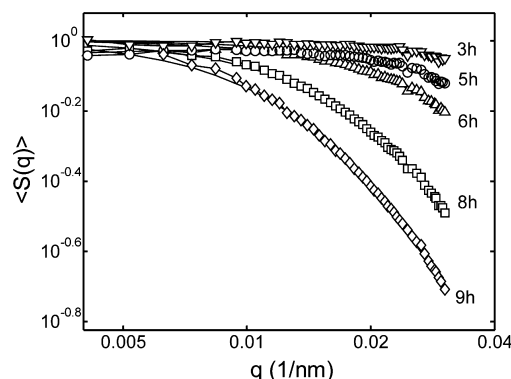

Figure 6. Time evolution of the structure factor of a 1 g/L protein sample incubated in 25 mM citric acid buffer at 37 °C and pH 3.0, with 0.15 M Na_2SO_4. Continuous lines are fitted curves according to eq 5.

interval, 16−150°, which is suitable for the analysis of the aggregates with radius of tens-hundreds nm produced during aggregation. Simultaneously, DLS was acquired on the same instrument at 145°. A 1 g/L protein solution in 25 mM citric acid buffer with 0.15 M Na_2SO_4 at pH 3.0 and 37 °C was selected as reference conditions. Using the Fisher-Burford formula for the structure factor of fractal aggregates

$$S(q) = \left(1 + \frac{2}{3D_f}(q\langle R_g\rangle)^2\right)^{-D_f/2}$$

(5)

the average gyration radius, $\langle R_g\rangle$, has been fitted to the experimental data using $D_f = 2.6$. This leads to the estimation of two independent moments of the cluster distribution, namely the average $\langle R_g\rangle$:

$$\langle R_g\rangle^2 = \frac{\sum_{i=1}^{N_{ag}} N_i m_i^2 R_{g,i}^2}{\sum_{i=1}^{N_{ag}} N_i m_i^2}$$

(6)

and the average $\langle R_h\rangle$

$$\langle R_h\rangle = \frac{\sum_{i=1}^{N_{ag}} N_i m_i^2 S_i(q)}{\sum_{i=1}^{N_{ag}} \frac{N_i m_i^2 S_i(q)}{R_{h,i}}}$$

(7)

where N_i, m_i and $S_i(q)$ are the number, mass and structure factor at the scattering vector q of aggregates containing i units, respectively.

The time evolution of $\langle R_g\rangle$ and $\langle R_h\rangle$ are reported in Figure 7. As expected, the two quantities are initially very similar but as aggregation proceeds $\langle R_g\rangle$ increases more rapidly than $\langle R_h\rangle$, being $\langle R_g\rangle$ a larger order moment of the cluster distribution, thus indicating the polidispersity of the distribution of the aggregate sizes.

Aggregation Model and Population Balance Equations. In a previous work[49] we investigated the early stages of antibody oligomerization in acidic conditions. The aggregation process was found to be reversible and well described by a modified Lumry−Eyring model, which included the denaturation of monomer followed by reversible formation of dimers and trimers.
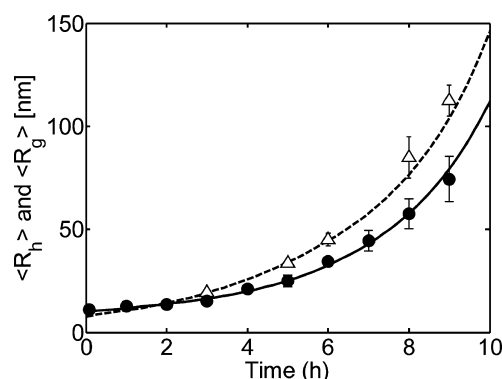

Figure 7. Values of the average radius of gyration $\langle R_g\rangle$ (Δ) and the average hydrodynamic radius $\langle R_h\rangle$ (●), measured experimentally as a function of the aggregation time. Continuous curve and dashed curve represent PBE model simulations of $\langle R_h\rangle$ and $\langle R_g\rangle$ computed using the RLCA kernel (eq 12), respectively.

In this work, we have seen that at higher temperatures the oligomers (i.e., aggregates containing few monomer units) are no longer stable, and aggregate with monomer and other oligomers to form larger aggregates. While, as mentioned above, the aggregation steps involving monomer are reversible, the aggregation between oligomers and larger aggregates (which can be defined together as clusters) is irreversible. Thus, summarizing, the aggregation process can be described with the reaction scheme shown in Figure 8. The aggregation is
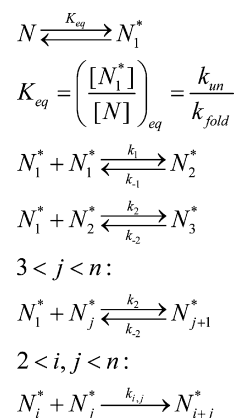
$$N \xrightleftharpoons{K_{eq}} N_1^*$$

$$K_{eq} = \left(\frac{[N_1^*]}{[N]}\right)_{eq} = \frac{k_{un}}{k_{fold}}$$

$$N_1^* + N_1^* \underset{k_{-1}}{\overset{k_1}{\rightleftharpoons}} N_2^*$$

$$N_1^* + N_2^* \underset{k_{-2}}{\overset{k_2}{\rightleftharpoons}} N_3^*$$

$$3 < j < n:$$

$$N_1^* + N_j^* \underset{k_{-2}}{\overset{k_2}{\rightleftharpoons}} N_{j+1}^*$$

$$2 < i, j < n:$$

$$N_i^* + N_j^* \xrightarrow{k_{i,j}} N_{i+j}^*$$

Figure 8. Kinetic scheme of the aggregation process based on a modified Lumry−Eyring model.

initiated by the formation of a reactive intermediate with a metastable conformation, N_1^*, from the antibody in the native form, N. Such intermediate can aggregate reversibly both with other monomeric intermediates (N_1^*) and with oligomers (N_2^*, N_3^*, ...). We distinguish the reactivity between two monomers and between a monomer and an oligomer by introducing two different sets of rate constants: k_1 and k_{-1}, and k_2 and k_{-2}, describing the forward and the backward aggregation rate constants for monomer−monomer and monomer−oligomer aggregation, respectively. It is worth noticing that k_1 and k_2 are rate constants of reactions which lump together the equilibrium between native (N) and intermediate (N_1^*) state of the protein, and the following propagation step.[49] The irreversible aggregation between two generic clusters containing i and j units is described by the aggregation rate constant k_{ij}.

From this kinetic scheme, the following population balance equations have been derived for intermediate monomer, N_1^*, dimer, N_2^*, trimer, N_3^*, and the generic cluster containing i units (N_i^*):

$$\frac{dN_1^*}{dt} = -2k_1 N_1^{*2} + 2k_{-1} N_2^* - k_2 N_1^* \left(\sum_\infty (N_j^*) \right)$$
$$+ k_{-2} \sum_\infty^{i=3} (N_i^*) \tag{8}$$

$$\frac{dN_2^*}{dt} = k_1 N_1^{*2} - k_{-1} N_2^* - k_2 N_1^* N_2^* + k_{-2} N_3^*$$
$$- N_2^* \left(\sum_\infty^{j=2} k_{2,j} N_j^* \right) \tag{9}$$

$$\frac{dN_3^*}{dt} = k_2 N_1^* N_2^* - k_{-2} N_3^* - k_2 N_1^* N_3^* + k_{-2} N_4^*$$
$$- N_3^* \left(\sum_\infty^{j=2} k_{3,j} N_j^* \right) \tag{10}$$

$i > 3$

$$\frac{dN_i^*}{dt} = \frac{1}{2} \sum_{i-1}^{j=2} k_{j,i-j} N_j^* N_{i-j}^* - N_i^* \sum_\infty^{j=2} k_{i,j} N_j^*$$
$$- k_2 N_1^* N_i^* + k_{-2} N_{i+1}^* \tag{11}$$

With reference to a given population of clusters, N_i^*, the terms on the right side of eq 11 represent on one hand its increase by aggregation of smaller clusters and on the other its decrease due to reaction with other aggregates. It is worth noticing that eqs 8−11 represent essentially a generalization of the Smoluchowski's population balance equations[50] to account for the reversibility of oligomer formation and the different values of the kinetic rate constants describing monomer−monomer, monomer−cluster, and cluster−cluster aggregation.

Let us consider the coagulation kinetics at pH 3.0 and 37 °C with 0.15 M Na_2SO_4 (Figure 1a): it appears that under these conditions the reversible nucleation of oligomers is confined to the very early stages of the process. This is confirmed by size exclusion chromatography measurements which show a small amount of residual monomeric antibody after 1 h of incubation (data not shown).

Accordingly, in this case we can neglect the nucleation step and assume that the coagulation starts from a homogeneous population of oligomers with $\langle R_h \rangle = 9$ nm, corresponding to trimers. Which implies, in eq 8-11, to set N_1 and N_2 equal to zero. Then, the PBEs reduce to

$$\frac{dN_i^*}{dt} = \frac{1}{2} \sum_{i-1}^{j=2} k_{j,i-j} N_j^* N_{i-j}^* - N_i^* \sum_\infty^{j=2} k_{i,j} N_j^*, \quad i \geq 3 \tag{12}$$

The solution of the PBEs involves the choice of the aggregation kernel, k_{ij}. When no repulsive barrier exists among the proteins, the process is controlled by Brownian motions and aggregation occurs under fast, diffusion limited conditions (DLCA). On the other hand, when an energetic barrier stabilizes two approaching particles, the aggregation efficiency is reduced, the system is under reactive limited conditions

(RLCA) and shows lower coagulation rates. The general kernel for RLCA aggregation of fractal objects is

$$k_{i,j} = \frac{k_B}{W} B_{i,j} P_{i,j} \tag{13}$$

where k_B is the Smoluchowski rate constant for diffusion limited aggregation, defined as follows: $k_B = 8kT/3\eta$, where k is the Boltzmann constant, T is the temperature, and η is the viscosity. W is the so-called stability ratio, accounting for the energetic barrier between two approaching primary particles, $B_{i,j}$ is the correction for the Brownian term that accounts for the fractal nature of the aggregates and for the aggregation between unequal size clusters:

$$B_{i,j} = \frac{(i^{1/D_f} + j^{1/D_f}) \left(\frac{1}{i^{1/D_f}} + \frac{1}{j^{1/D_f}} \right)}{4} \tag{14}$$

where the experimentally measured fractal dimension of $D_f = 2.6$ has been used. Finally, $P_{i,j}$ is the correction term for RLCA conditions with respect to DLCA conditions. Several expressions of $P_{i,j}$ have been proposed in the literature.[51] In the absence of precise information about the relationship between aggregates structure and reactivity, we selected the product kernel:[52]

$$P_{i,j} = (ij)^\lambda \tag{15}$$

which includes the entire size dependence of the RLCA aggregation rate in a semiempirical parameter λ, which based on purely fractal scaling arguments is expected to be in the order of $1 - 1/D_f$ and therefore, with $D_f = 2.6$, $\lambda = 0.61$.[53]

The system of ODEs (eqs 8−11) has been solved numerically using the algorithm proposed by Kumar and Ramkrishna.[51,54,55] Both DLCA and RLCA kernels were tested by comparing model simulations to the experimental data of the time evolution of $\langle R_h \rangle$ and $\langle R_g \rangle$. While the DLCA predicted an aggregation time in the order of milliseconds and therefore far away from the experimental data, a satisfactory agreement was obtained using the RLCA kernel with fitting parameters $\lambda = 0.6 \pm 0.01$ and $W = 3.3 \pm 0.1 \times 10^8$, as shown in Figure 7. The mean squared error, defined as $E = \sum_{i=1}^N (y_i - y_{i,est})^2/N$, where y represents the measured normalized average radius of hydration and gyration, y_{est} the variable estimated by the model and N the number of experimental points, is $2.5 \pm 0.2 \times 10^{-3}$. It is worth noticing that the fitted value $\lambda = 0.6$ is very close to the expected value of 0.61 estimated above through fractal scaling arguments. The model simulations are in reasonable agreement with the experimental data, although the time evolution of $\langle R_h \rangle$ and $\langle R_g \rangle$ are slightly over- and underestimated, respectively. Since the difference between these two average moments is related to the polydispersity of the distribution, this indicates that the experimental distributions are broader than the simulated ones.

It is worth noticing that the estimated value of $W = 3.3 \times 10^8$ is close to the value $W = 9.1 \times 10^8$ previously reported in the literature for antibody aggregation induced at neutral pH and large temperature.[48] These large W values indicate that protein aggregates are significantly stabilized, even in non-native conditions.

Equation 12 can be conveniently expressed in dimensionless form

$$\frac{dX_i}{d\tau} = \frac{1}{2} \sum_{i-1}^{j=2} \beta_{i,j} X_j X_{i-j} - X_i \sum_{\infty}^{j=2} \beta_{i,j} X_j \qquad (16)$$

where X_i is the dimensionless cluster number concentration $X_i = N_i/N_{1,0}$, with $N_{1,0}$ the initial number concentration of protein particles, $\beta_{i,j} = B_{i,j} P_{i,j}$ and $\tau = t/t_C$ is the dimensionless time normalized with respect to the characteristic aggregation time, t_C, defined as:

$$\frac{1}{t_C} = \frac{1}{W} k_B N_{1,0} \qquad (17)$$

From the dimensionless form of the PBE (eq 16) it can be seen that the time evolution of the cluster distribution depends only on the two parameters D_f and λ, included in $B_{i,j}$ and $P_{i,j}$, respectively. This implies that, if the aggregation process produces clusters with the same structure (D_f and λ), the aggregation kinetics (e.g., the time evolution of the average hydrodynamic radius) follows a single master curve when plotted versus the dimensionless time, τ, independently on the particle material, particle concentration and conditions of aggregation. This has been shown in the past for polymeric colloidal systems in RLCA and DLCA conditions.[51,56,57]

Let us consider now the aggregation kinetics under various different conditions reported in Figure 1. We see that the aggregation time scales vary quite a bit, ranging from a few hours (Figure 1, parts a and b) to several days (Figure 1c). However, when introducing the dimensionless time, τ, and using W as a fitting parameter, all the different kinetic profiles collapse on a single master curve, as shown in Figure 9. This important result indicates that, at least in the conditions investigated in this work, aggregation follows a unique mechanism well represented by the adopted kinetic scheme of aggregation and kernel model. It is worth noticing that this conclusion applies for various conditions at acidic pH: several temperatures at fixed pH (Figure 9a), several counterions at fixed temperature and pH (Figure 9b) and different salt concentrations at different pH (Figure 9b). The analysis was extended to two studies reported in the literature, which describe a coagulation mechanism similar the one observed in this work: a 10 g/L IgG1 solution at physiological pH 6.5 at 60 °C,[58] and 1 g/L IgG1 solution at pH 4.5 and 58 °C.[30] In Figure 9c it can be seen that these antibodies behave similarly to the IgG investigated in this work and in fact collapse on the same master curve. The results shown in Figure 9 indicate a certain level of generality in the antibody aggregation behavior, at least when condensation mechanism dominates chain polymerization.

The W values estimated for all the different conditions investigated in Figure 9 are reported in Table 1. The quantification of W allows some important considerations: the large W values in all conditions indicate that even in non-native conditions aggregation of immunoglobulins is not under diffusive control, but rather it is an activated process with some energy barrier to be overcome for aggregation to occur. In Figure 10 the effective cluster kinetic rate coefficients, $k_C = k_B/W$, is shown as a function of the reciprocal temperatures: it is seen that in the investigated temperature range, the kinetics follows Arrhenius law, with an effective activation energy of 60 kcal/mol.

Another interesting comparison can be made by considering that in the kernel expression of eq 13 the effect of the aggregate size i and j is confined in the terms B_{ij} and P_{ij}, while the Fuchs
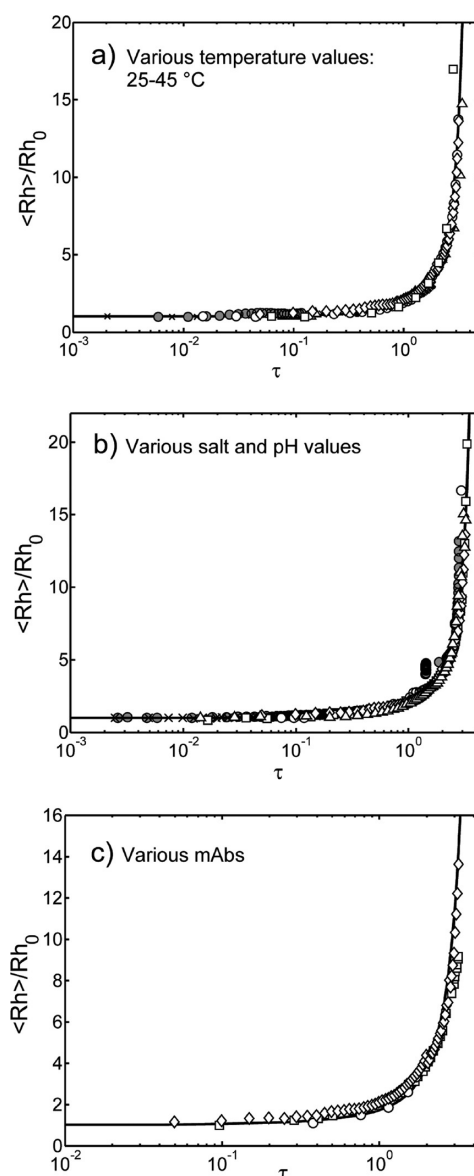

Figure 9. (a) Time evolution of the normalized average hydrodynamic radius versus dimensionless time for a 1 g/L mAb solution in 25 citric acid buffer at pH 3.0 and with 0.15 M Na_2SO_4 at: 25 °C (Δ), 30 °C ($\bullet$), 35 °C ($\times$), 37 °C ($\Diamond$), 39 °C ($\bigcirc$), 45 °C ($\square$). (b) Same as part a but at pH 3.0 and 37 °C with 0.15 M NaH_2PO_4 ($\times$), NaCl ($\bullet$), Na_2SO_4 ($\Diamond$), $NaNO_3$ (Δ), at pH 4.0 and 55 °C with 0.15 M Na_2SO_4 ($\square$), and at pH 3.0 and 25 °C with 0.5 M NaCl ($\bigcirc$). (c) Kinetics data of model IgG of this work ($\Diamond$) are compared to data of other antibodies taken from ref 58 ($\bigcirc$) and ref 30 ($\square$) (see main text for details). The continuous lines represent model simulations.

stability ratio W refers to primary particles, i.e. to the aggregation between two oligomers containing one monomer unit. Therefore, this in principle should correspond to the kernel k_1. However, this cannot be the case because eq 13 does not account for structure changes which are particularly strong when going from N_1^* to N_2^*, N_3^* and then larger oligomers. This is in fact the rational why in the kinetic scheme in Figure 9 the aggregation kernel of the first three oligomers have been treated separately from that of larger oligomers. It is now interesting to compare such W, representing the stability of "oligomer of size one", with $W_1 = k_B/k_1$, which represents the stability of the non-native monomer species. This should reflect

Table 1. Effective Stability Ratio Values (W) Obtained by Scaling the Dimensionless Time Evolution of $\langle R_h \rangle$ in Various Conditions and with Different Antibodies on a Single Master Curve, as Shown in Figure 9[a]

	W					
	25 °C	30 °C	35 °C	37 °C	39 °C	45 °C
pH 3.0 and 0.15 M Na$_2$SO$_4$ at various temperatures	1.7×10^{10}	2.5×10^{9}	5.1×10^{8}	3.3×10^{8}	1.7×10^{8}	4.3×10^{7}
		NaH$_2$PO$_4$	NaCl		Na$_2$SO$_4$	NaNO$_3$
pH 3.0 and 37 °C, with 0.15 M solutions of various salts		6.3×10^{9}	2.5×10^{9}		3.3×10^{8}	2.2×10^{8}
other conditions						
pH 4.0 and 55 °C, with 0.15 M Na$_2$SO$_4$					3.0×10^{8}	
pH 3.0 and 25 °C, with 0.5 M NaCl					1.8×10^{10}	
ref 58. IgG1, pH 6.5 and 60 °C					2.5×10^{9}	
ref 30. IgG1, pH 4.5 and 58 °C					7.2×10^{8}	

[a]The average uncertainty of the fitted parameters is ±5% of the value.
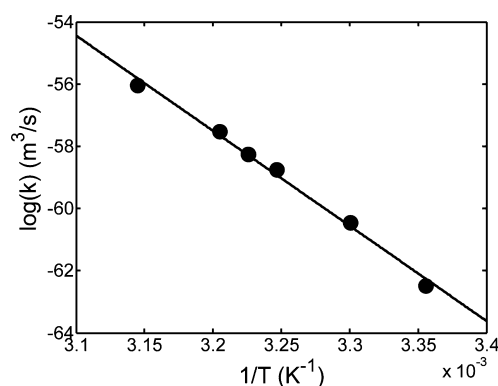
Figure 10. Arrhenius plot of the effective kinetic rate constants, $k_C = k_B/W$, at pH 3.0 with 0.15 M Na$_2$SO$_4$ evaluated from the W values reported in Table 1. The fitting provides an activation energy of 60 kcal/mol.

the different stability character of oligomers and monomers depurated from the size effect. For this, the oligomerization rate constant, k_1, at 25 °C and low protein concentration (0.1−0.5 g/L) for chloride was used as reported in ref49., while for the other anions it was measured using the same procedure (the summary of the procedure is reported in the Supporting Information). The obtained W and W_1 values are compared in Figure 11. It is seen that the anion effect on the interactions between two non-native monomers is reflected in the interactions between two non-native aggregates. Moreover,
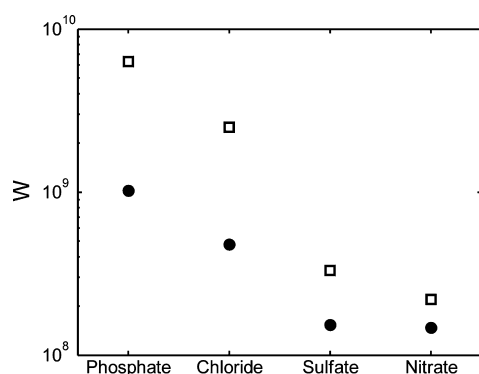
Figure 11. Effective interaction potential between two non-native mAb monomers, W_1, at 25 °C (●), and between two mAb aggregates, W, at 37 °C (□) in 25 mM citric acid buffer at pH 3.0 with 0.15 M of different sodium salts.

the stability ratios are smaller for monomers at 25 °C than for aggregates at 37 °C, indicating a significantly larger reactivity for the monomers. For the aggregation at pH 3.0 with 0.15 M Na$_2$SO$_4$ at 25 °C W_1 and W were in fact found equal to $W_1 = 1.5 \times 10^8$ (Figure 11) and $W = 1.7 \times 10^{10}$ (Table 1), i.e. a difference of 2 orders of magnitude.

We conclude that the incubation of antibody at pH 3.0 induces formation of a reactive non-native structure which exposes aggregating-prone (likely hydrophobic) patches; during aggregation, the number of these patches reduces and, consequently, the reactivity of aggregates is lower than that of monomers. The transition in reactivity occurs sharply within few aggregating units, together with the change in secondary structure of the oligomers.

■ CONCLUSIONS

We investigated the aggregates morphology and aggregation kinetics of a model IgG2 in acidic conditions. It was found that antibody aggregates exhibit an effective fractal morphology, with fractal dimension equal to 2.6, in agreement with TEM pictures.

Two average moments of the cluster distribution, namely the average radius of gyration, $\langle R_g \rangle$, and the average hydrodynamic radius, $\langle R_h \rangle$, have been measured in situ by light scattering. A comprehensive population balance model based on modified Smoluchowski equations has been developed to describe the two-step aggregation process: reversible oligomerization followed by cluster−cluster aggregation. The model simulations are in good agreement with experimental data, and indicate that non-native antibody aggregation does not occur under diffusive control, i.e. it is an activated process.

Introducing a dimensionless time scaled on the Fuchs stability ratio (W), the time evolutions of $\langle R_h \rangle$ measured under a great variety of operating conditions (temperature, pH, type, and concentration of salt) collapse on a single master curve. This applies also to data reported in the literature when growth by cluster−cluster coagulation dominates, indicating a certain level of generality in the antibodies aggregation behavior.

The described analysis gives important quantitative information on the effective protein−protein interactions and their dependence on operating parameters, such as temperature, pH, and type of anion. In particular, it is found that the aggregation rate increases with increasing temperature according to an Arrhenius law. Moreover, the reactivity of the aggregates is lower than the one of the intermediate monomers. This is likely due to the reduction during aggregation of the number of

available, aggregating-prone (hydrophobic) patches induced by monomer unfolding at pH 3.0.

■ ASSOCIATED CONTENT

ⓢ Supporting Information

Description of the procedure for the evaluation of the oligomerization rate constants. This material is available free of charge via the Internet at http://pubs.acs.org.

■ AUTHOR INFORMATION

Corresponding Author
*E-mail: massimo.morbidelli@chem.ethz.ch.

Notes
The authors declare no competing financial interest.

■ ACKNOWLEDGMENTS

■ REFERENCES

(1) Chiti, F.; Dobson, C. M. *Annu. Rev. Biochem.* **2006**, *75*, 333−366.

(2) Wang, W. *Int. J. Pharm.* **2005**, *289*, 1−30.

(3) Aggarwal, S. *Nat. Biotechnolog.* **2008**, *26*, 1227−1233.

(4) Mahler, H.-C.; Friess, W.; Grauschopf, U.; Kiese, S. *J. Pharm. Sci.* **2009**, *98*, 2909−2934.

(5) Lomakin, A.; Chung, D. S.; Benedek, G. B.; Kirschner, D. A.; Teplow, D. B. *Proc. Natl. Acad. Sci. U.S.A.* **1996**, *93*, 1125−1129.

(6) Serio, T. R.; Cashikar, A. G.; Kowal, A. S.; Sawicki, G. J.; Moslehi, J. J.; Serpell, L.; Arnsdorf, M. F.; Lindquist, S. L. *Science* **2000**, *289*, 1317−1321.

(7) Uversky, V. N.; Fink, A. L. *BBA-Proteins Proteom.* **2004**, *1698*, 131−153.

(8) Uversky, V. N.; Fernandez, A.; Fink, A. L. *Protein Reviewes, Vol.4: Protein Misfolding, Aggregation and Conformational Diseases*; Springer Science: Singapore, 2006.

(9) Chiti, F.; Stefani, M.; Taddei, N.; Ramponi, G.; Dobson, C. M. *Nature* **2003**, *424*, 805−808.

(10) Krebs, M. R. H.; Devlin, G. L.; Donald, A. M. *Biophys. J.* **2007**, *92*, 1336−1342.

(11) Faendrich, M.; Schmidt, M.; Grigorieff, N. *Trends Biochem. Sci.* **2011**, *36*, 338−345.

(12) Walsh, D. M.; Klyubin, I.; Fadeeva, J. V.; Cullen, W. K.; Anwyl, R.; Wolfe, M. S.; Rowan, M. J.; Selkoe, D. J. *Nature* **2002**, *416*, 535−539.

(13) Gimel, J. C.; Durand, D.; Nicolai, T. *Macromolecules* **1994**, *27*, 583−589.

(14) Morris, A. M.; Watzky, M. A.; Finke, R. G. *BBA-Proteins Proteom.* **2009**, *1794*, 375−397.

(15) Roberts, C. J. *J. Phys. Chem. B* **2003**, *107*, 1194−1207.

(16) Powers, E. T.; Powers, D. L. *Biophys. J.* **2008**, *94*, 379−391.

(17) Lee, C.-C.; Nayak, A.; Sethuraman, A.; Belfort, G.; McRae, G. J. *Biophys. J.* **2007**, *92*, 3448−3458.

(18) Oosawa, F.; Kasai, M. *J. Mol. Biol.* **1962**, *4*, 10−21.

(19) Ferrone, F. *Method Enzymol.* **1999**, *309*, 256−274.

(20) Kayser, V.; Chennamsetty, N.; Voynov, V.; Helk, B.; Forrer, K.; Trout, B. L. *J. Pharm. Sci.* **2011**, *100*, 2526−2542.

(21) Roberts, C. J. *Biotechnol. Bioeng.* **2007**, *98*, 927−938.

(22) Weiss, W. F.; Young, T. M.; Roberts, C. J. *J. Pharm. Sci.* **2009**, *98*, 1246−1277.

(23) Andrews, J. M.; Roberts, C. J. *J. Phys. Chem. B* **2007**, *111*, 7897−7913.

(24) Li, Y.; Roberts, C. J. *J. Phys. Chem. B* **2009**, *113*, 7020−7032.

(25) Li, Y.; Ogunnaike, B. A.; Roberts, C. I. *J. Pharm. Sci.* **2010**, *99*, 645−662.

(26) Andrews, J. M.; Roberts, C. J. *Biochemistry* **2007**, *46*, 7558−7571.

(27) Roberts, C. J.; Darrington, R. T.; Whitley, M. B. *J. Pharm. Sci.* **2003**, *92*, 1095−1111.

(28) Sahin, E.; Grillo, A. O.; Perkins, M. D.; Roberts, C. J. *J. Pharm. Sci.* **2010**, *99*, 4830−4848.

(29) Brummitt, R. K.; Nesta, D. P.; Chang, L. Q.; Chase, S. F.; Laue, T. M.; Roberts, C. J. *J. Pharm. Sci.* **2011**, *100*, 2087−2103.

(30) Brummitt, R. K.; Nesta, D. P.; Chang, L. Q.; Kroetsch, A. M.; Roberts, C. J. *J. Pharm. Sci.* **2011**, *100*, 2104−2119.

(31) Hiemenz., P., C. *Principles of colloid and surface chemistry*; Marcel Dekker: New York, 1986.

(32) Cohen, S. I. A.; Vendruscolo, M.; Welland, M. E.; Dobson, C. M.; Terentjev, E. M.; Knowles, T. P. J. *J. Chem. Phys.* **2011**, *135* (065105), 1−16.

(33) Knowles, T. P. J.; Waudby, C. A.; Devlin, G. L.; Cohen, S. I. A.; Aguzzi, A.; Vendruscolo, M.; Terentjev, E. M.; Welland, M. E.; Dobson, C. M. *Science* **2009**, *326*, 1533−1537.

(34) Murphy, R. M.; Pallitto, M. R. *J. Struct. Biol.* **2000**, *130*, 109−122.

(35) Piazza, R. *Curr. Opin. Colloid In.* **2000**, *5*, 38−43.

(36) Curtis, R. A.; Lue, L. *Chem. Eng. Sci.* **2006**, *61*, 907−923.

(37) Chennamsetty, N.; Voynov, V.; Kayser, V.; Helk, B.; Trout, B. L. *Proc. Natl. Acad. Sci. U.S.A.* **2009**, *106*, 11937−11942.

(38) Chi, E. Y.; Krishnan, S.; Randolph, T. W.; Carpenter, J. F. *Pharm. Res.* **2003**, *20*, 1325−1336.

(39) Shammas, S. L.; Knowles, T. P. J.; Baldwin, A. J.; MacPhee, C. E.; Welland, M. E.; Dobson, C. M.; Devlin, G. L. *Biophys. J.* **2011**, *100*, 2783−2791.

(40) Fast, J. L.; Cordes, A. A.; Carpenter, J. F.; Randolph, T. W. *Biochemistry* **2009**, *48*, 11724−11736.

(41) Chi, E. Y.; Krishnan, S.; Kendrick, B. S.; Chang, B. S.; Carpenter, J. F.; Randolph, T. W. *Protein Sci.* **2003**, *12*, 903−913.

(42) Chi, E. Y.; Kendrick, B. S.; Carpenter, J. F.; Randolph, T. W. *J. Pharm. Sci.* **2005**, *94*, 2735−2748.

(43) Olsen, S. N.; Andersen, K. B.; Randolph, T. W.; Carpenter, J. F.; Westh, P. *BBA-Proteins Proteom.* **2009**, *1794*, 1058−1065.

(44) Javid, N.; Vogtt, K.; Krywka, C.; Tolan, M.; Winter, R. *Phys. Rev. Lett.* **2007**, *99* (028101), 1−4.

(45) Modler, A. J.; Gast, K.; Lutsch, G.; Damaschun, G. *J. Mol. Biol.* **2003**, *325*, 135−148.

(46) Arosio, P.; Owczarz, M.; Müller-Späth, T.; Rognoni, P.; Beeg, M.; Wu, H.; Salmona, M.; Morbidelli, M. *PLoS One* **2012**, *7* (e33372), 1−12.

(47) Lee, H.; Kirchmeier, M.; Mach, H. *J. Pharm. Sci.* **2011**, *100*, 416−423.

(48) Feder, J.; Jossang, T.; Rosenqvist, E. *Phys. Rev. Lett.* **1984**, *53*, 1403−1406.

(49) Arosio, P.; Barolo, G.; Muller-Spath, T.; Wu, H.; Morbidelli, M. *Pharm. Res.* **2011**, *28*, 1884−1894.

(50) von Smoluchowski, M. *Z. Phys. Chem.-Stoch. Ve.* **1917**, *92*, 129−168.

(51) Lattuada, M.; Sandkuhler, P.; Wu, H.; Sefcik, J.; Morbidelli, M. *Adv. Colloid Interfac.* **2003**, *103*, 33−56.

(52) Family, F.; Meakin, P.; Vicsek, T. *J. Chem. Phys.* **1985**, *83*, 4144−4150.

(53) Schmitt, A.; Odriozola, G.; Moncho-Jorda, A.; Callejas-Fernandez, J.; Martinez-Garcia, R.; Hidalgo-Alvarez, R. *Phys. Rev. E* **2000**, *62*, 8335−8343.

(54) Kumar, S.; Ramkrishna, D. *Chem. Eng. Sci.* **1996**, *51*, 1311−1332.

(55) Kumar, S.; Ramkrishna, D. *Chem. Eng. Sci.* **1996**, *51*, 1333−1342.

(56) Sandkuhler, P.; Sefcik, J.; Morbidelli, M. *J. Phys. Chem. B* **2004**, *108*, 20105−20121.

(57) Sandkuhler, P.; Sefcik, J.; Morbidelli, M. *Langmuir* **2005**, *21*, 2062−2077.

(58) Andersen, C. B.; Manno, M.; Rischel, C.; Thorolfsson, M.; Martorana, V. *Protein Sci.* **2010**, *19*, 279–290.

7075

dx.doi.org/10.1021/jp301091n | *J. Phys. Chem. B* 2012, 116, 7066–7075